

Magnetic domain structures in ultrathin $Bi_2Te_3/CrTe_2$ heterostructures

Tirui Xia(夏体瑞), Xiaotian Yang(杨笑天), Yifan Zhang(张逸凡), Xinqi Liu(刘馨琪), Xinyu Cai(蔡新雨), Chang Liu(刘畅), Qi Yao(姚岐), Xufeng Kou(寇煦丰), and Wenbo Wang(王文波)
Citation: Chin. Phys. B, 2024, 33 (**8**): 087504. DOI: 10.1088/1674-1056/ad4a3a

What follows is a list of articles you may be interested in

Critical behavior of quasi-two-dimensional ferromagnet $Cr_{1.04}Te_2$

Wei Niu(钮伟), Qin-Xin Song(宋沁心), Shi-Qi Chang(常世琦), Min Wang(王敏), Kui Yuan(袁奎), Jia-Cheng Gao(高嘉程), Shuo Wang(王硕), Zhen-Dong Wang(王振东), Kai-Fei Liu(刘凯斐), Ping Liu(刘萍), Yong-Bing Xu(徐永兵), Xiao-Qian Zhang(张晓倩), and Yong Pu(普勇)
Chin. Phys. B, 2024, 33 (**7**): 077506. DOI: 10.1088/1674-1056/ad4cd8

Multi-segmented nanowires for vortex magnetic domain wall racetrack memory

M Al Bahri, M Al Hinaai, and T Al Harthy
Chin. Phys. B, 2023, 32 (**12**): 127508. DOI: 10.1088/1674-1056/acca0a

Prediction of $LiCrTe_2$ monolayer as a half-metallic ferromagnet with a high Curie temperature

Li-Man Xiao(肖丽蔓), Huan-Cheng Yang(杨焕成), and Zhong-Yi Lu(卢仲毅)
Chin. Phys. B, 2023, 32 (**5**): 057505. DOI: 10.1088/1674-1056/acbe2e

Structural evolution-enabled $BiFeO_3$ modulated by strontium doping with enhanced dielectric, optical and superparamagnetic properties by a modified sol-gel method

Sharon V S, Veena Gopalan E, and Malini K A
Chin. Phys. B, 2023, 32 (**3**): 037504. DOI: 10.1088/1674-1056/ac785b

Thickness-dependent magnetic properties in $Pt/[Co/Ni]_n$ multilayers with perpendicular magnetic anisotropy

Chunjie Yan(晏春杰), Lina Chen(陈丽娜), Kaiyuan Zhou(周恺元), Liupeng Yang(杨留鹏), Qingwei Fu(付清为), Wenqiang Wang(王文强), Wen-Cheng Yue(岳文诚), Like Liang(梁力克), Zui Tao(陶醉), Jun Du(杜军),Yong-Lei Wang(王永磊), and Ronghua Liu(刘荣华)
Chin. Phys. B, 2023, 32 (**1**): 017503. DOI: 10.1088/1674-1056/ac5c37

Magnetic domain structures in ultrathin $Bi_2Te_3/CrTe_2$ heterostructures

Tirui Xia(夏体瑞)[1], Xiaotian Yang(杨笑天)[1], Yifan Zhang(张逸凡)[2,3], Xinqi Liu(刘馨琪)[1,3], Xinyu Cai(蔡新雨)[1], Chang Liu(刘畅)[4], Qi Yao(姚岐)[1,3,†], Xufeng Kou(寇煦丰)[2,3,‡], and Wenbo Wang(王文波)[1,3,§]

[1] *School of Physical Science and Technology, ShanghaiTech University, Shanghai* 201210, *China*
[2] *School of Information Science and Technology, ShanghaiTech University, Shanghai* 201210, *China*
[3] *ShanghaiTech Laboratory for Topological Physics, ShanghaiTech University, Shanghai* 201210, *China*
[4] *Department of Materials Science, Fudan University, Shanghai* 200438, *China*

(Received 27 February 2024; revised manuscript received 9 May 2024; accepted manuscript online 13 May 2024)

Chromium tellurium compounds are important two-dimensional van der Waals ferromagnetic materials with high Curie temperature and chemical stability in air, which is promising for applications in spintronic devices. Here, high-quality spin–orbital-torque (SOT) device, $Bi_2Te_3/CrTe_2$ heterostructure was epitaxially grown on Al_2O_3 (0001) substrates. Anomalous Hall measurements indicate the existence of strong ferromagnetism in this device with the $CrTe_2$ thickness down to 10 nm. In order to investigate its micromagnetic structure, cryogenic magnetic force microscope (MFM) was utilized to measure the magnetic domain evolutions at various temperatures and magnetic fields. The virgin domain state of the device shows a worm-like magnetic domain structure with the size around 0.6 μm–0.8 μm. Larger irregular-shape magnetic domains (>1 μm) can be induced and pinned, after the field is increased to coercive field and ramped back to low fields. The temperature-dependent MFM signals exhibit a nice mean-field-like ferromagnetic transition with Curie temperature around 201.5 K, indicating a robust ferromagnetic ordering. Such a device can be potentially implemented in future magnetic memory technology.

Keywords: $CrTe_2$, magnetic domain, magnetic force microscopy

PACS: 75.70.–I, 75.60.–d, 75.47.–m, 85.70.–w **DOI:** 10.1088/1674-1056/ad4a3a

1. Introduction

Since the discovery of two-dimensional (2D) ferromagnetism in $Cr_2Ge_2Te_6$[1] and CrI_3,[2] 2D magnetic materials have recently drawn tremendous attentions because of their unique properties. 2D layered materials with van der Waals force bonds can be artificially combined to form novel heterostructures[3] and twisted layered structures with intriguing quantum phenomena, such as orbital magnetism,[4] superconductivity,[5,6] and quantum anomalous Hall effect.[7] Transition metal dichalcogenides (TMDs) comprise a large family of materials with chemical formula MX_2, where M is a transition metal atom (such as V, Cr, Mn, W or Mo) and X is a chalcogen atom (such as S, Se or Te). Magnetic TMDs exhibit excellent magnetic properties of low-dimensional materials and have great potential applications in spintronic devices. Among the large family of magnetic TMDs, chromium tellurium compounds with different compositions have been extensively studied.[8–28] Some appealing phenomena have been discovered in this material system, such as skyrmions,[19] biskyrmions,[20] colossal anomalous Hall effect (CAHE),[11,22] and planar Hall effect.[26] Moreover, these materials have shown outstanding magnetic properties at near-ambient conditions, making it promising to be utilized in industrial devices. For instance, a high-quality 2D Cr_5Te_8 nanosheets on mica substrate was synthesized via chemical vapor deposition (CVD) and their robust magneto-optical Kerr effect (MOKE) signals remain almost unchanged after three months of aging in air.[23] Using element-selective x-ray magnetic imaging and magnetic force microscopy (MFM) techniques, magnetic domains and Néel-like domain walls in micron-sized flakes of the $CrTe_2$ vdW ferromagnet were resolved at room temperature.[12] Recently, a thickness-dependent ferromagnetism in epitaxially grown Cr_2Te_3 thin films was reported.[18] Even in the strict 2D limit, the monolayer Cr_2Te_3 still retains the ferromagnetism despite the reduction in T_c due to the dimensionality effect. These results pave the way for optimizing the performance of 2D ferromagnetism for future applications.

High-quality 2D ferromagnets can be harnessed in magnetic random-access memory (MRAM) devices with the advantages of high durability, high speed, low power consumption, good miniaturization, and well-behaved device consistency.[29] In spin–orbital-torque (SOT) MRAM, the ferromagnetic layer is usually integrated with the strong spin–orbital coupling (SOC) layer, e.g., heavy metals and topological insulators.[30–34] Therefore, the magnetization can be reversed by flowing a current, instead of applying magnetic fields. Recently, wafer-scale $Bi_2Te_3/CrTe_2$ heterostructures

†Corresponding author. E-mail: yaoqi@shanghaitech.edu.cn
‡Corresponding author. E-mail: kouxf@shanghaitech.edu.cn
§Corresponding author. E-mail: wangwb1@shanghaitech.edu.cn

© 2024 Chinese Physical Society and IOP Publishing Ltd

have been grown on sapphire substrates by molecular beam epitaxy (MBE) and substantial switching power reduction has been achieved in this SOT device, providing a route for design of energy-efficient spintronics based on 2D ferromagnets. The low switching power ~ 8 mW/μm^3 and a high endurance of more than 5×10^4 write/read cycles have been experimentally demonstrated.[30] Magnetic domain structures in SOT devices are of high interest because they can be used as information storage unit. Although micromagnetic structures have been characterized on ultrathin CrTe crystals[8,12] and bulk Cr_5Te_8 crystals,[24] the systematic measurements of magnetic domains in CrTe-based SOT devices are still lacking.

In this work, high-quality $Bi_2Te_3/CrTe_2$ heterostructures were grown by molecular beam epitaxy (MBE), which was characterized by x-ray diffraction (XRD), Raman and atomic force microscope (AFM) techniques. The heterostructures were fabricated into Hall bar device for cryogenic MFM and transport measurements. Direct observation of magnetic domain structures at various magnetic fields and temperatures confirms a robust ferromagnetic long-range ordering in this heterostructures, which is consistent with the anomalous Hall measurements. Our micromagnetic studies of $Bi_2Te_3/CrTe_2$ heterostructure pave the way for utilizing SOT devices in next-generation magnetic-memory technology.

2. Experiments

The crystalline structure of $Bi_2Te_3/CrTe_2$ heterostructure with ferromagnetically ordered Cr spins was shown in Fig. 1(a). In 1T-phase of $CrTe_2$, Cr (green spheres) and Te (gray spheres) atoms with $P\bar{3}m1$ space group follow the Te–Cr–Te Z-shaped stacking configuration. Bi_2Te_3 layer with $R\bar{3}m$ space group grown on top of $CrTe_2$ layer, has Te–Bi–Te–Bi–Te stacking configuration. The $Bi_2Te_3/CrTe_2$ heterostructures were epitaxially grown on Al_2O_3 (0001) substrates by using an MBE system with a vacuum of 10^{-10} mbar (1 bar = 10^5 Pa). Prior to the sample growth, the Al_2O_3 substrate was heated at 600 °C in order to remove absorbed contamination. The Cr and Bi elements were evaporated from standard Knudsen effusion cells, while the Te elements were evaporated from a thermal cracker cell. The growth processes were monitored by the reflection high energy electron diffraction (RHEED). In order to determine its crystalline structure, high-resolution x-ray diffraction (XRD) was used to observe the diffraction peaks with the K_α x-ray of the Cu target. The XRD data in Fig. 1(b) shows only a series of $CrTe_2$ (00n) and Bi_2Te_3 (00n) diffraction peaks without any impurity phase and confirm the high-quality crystallinity of the $Bi_2Te_3/CrTe_2$ heterostructure on sapphire [Al_2O_3 (0001)] substrate, consistent with previous literature reports.[28] Raman spectra of the $CrTe_2$ nanosheets in Fig. 1(c) show two pristine characteristic peaks at 102.2 cm^{-1} and 136.6 cm^{-1} wave number, corresponding to the out-of-plane A_{1g} and in-plane E_g vibration modes, respectively. Such Raman peaks coincide well with the data reported in previous $CrTe_2$ studies.[13]

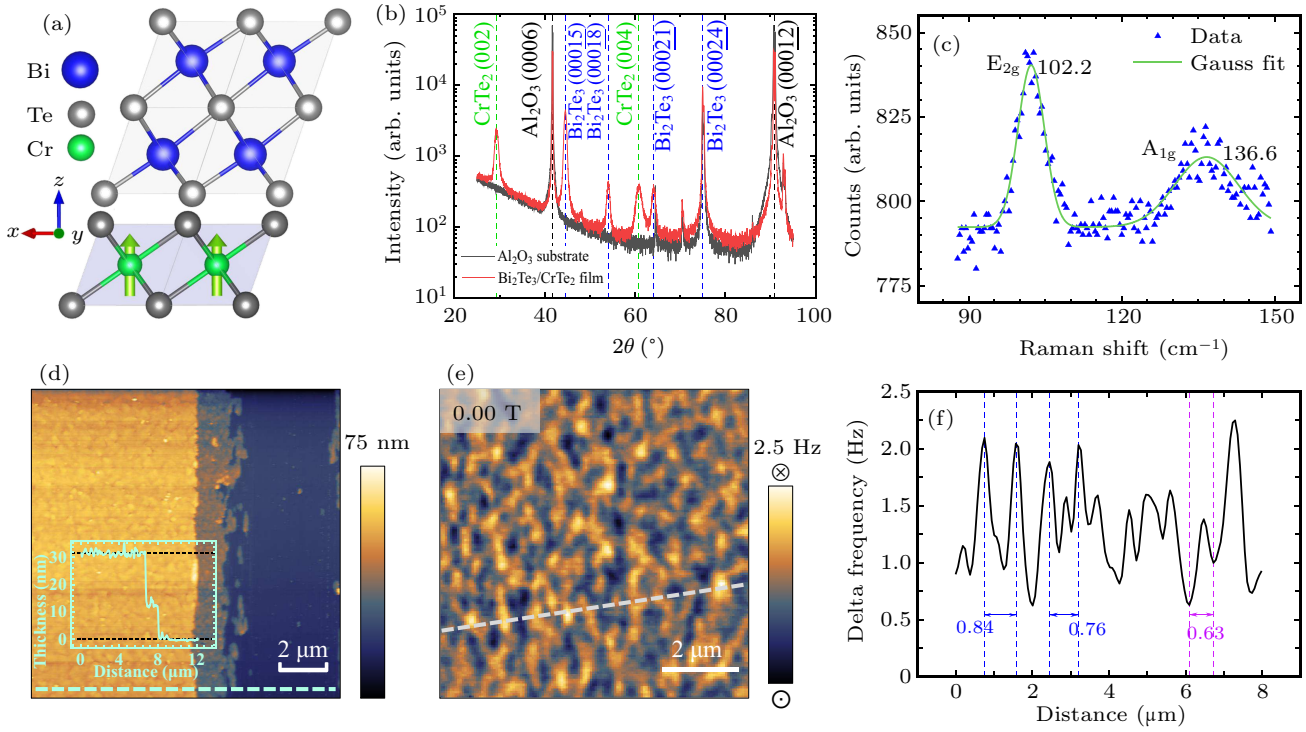


Fig. 1. (a) A schematic picture of crystal structure of $Bi_2Te_3/CrTe_2$ heterostructure. (b) XRD data of $Bi_2Te_3/CrTe_2$ heterostructure grown on Al_2O_3 (0001) substrates. (c) Raman data of $CrTe_2$ thin film. (d) AFM image on the sample edge of the heterostructure, inset shows the line profile along the dashed green line in panel (d). (e) After zero-field cooling process to 2 K, the MFM image taken at ground state after zero-field cooling to 2 K. (f) Line profile along the gray line in panel (e).

Room-temperature AFM (Cypher ES, Asylum Research) was used to characterize the roughness and thickness of the heterostructure. Hall bar device of $Bi_2Te_3/CrTe_2$ heterostructure (40 μm × 20 μm) was fabricated for MFM and transport measurements. The Hall and longitudinal resistances were measured by a lock-in amplifier (SR830) combined with a current source (Model 6221) providing an AC current around 1 μA. Cryogenic MFM measurements were performed in cryogen-free closed cycle cryostat (Attodry2100). Commercial magnetic probes (NanoWorld) were driven at resonance frequency ∼ 70.6 kHz and lifted ∼ 100 nm above the sample surface. The heterostructure was coated by ∼ 10-nm Au film and the tip was grounded with the sample surface to eliminated the possible electrostatic interaction. The resonance frequency shift which is scaled with the local field gradient was recorded as MFM signal. The blue and yellow areas in the MFM images represent up and down magnetic domains.

3. Results and discussion

In order to verify the thickness of the $Bi_2Te_3/CrTe_2$ heterostructure, its sharp step edge was exposed by hand scratch using a sharp tweezer. As shown in Fig. 1(d), the AFM image of the heterostructure shows a clean and flat surface with ∼ 1.8-nm roughness. The line-cut cross the sample edge, as shown in the inset, exhibits two sharp steps with the total thickness ∼ 30 nm. The top and bottom layers are roughly 20 nm and 10 nm respectively, which likely correspond to Bi_2Te_3 and $CrTe_2$ layers based on nominal thicknesses estimated from growth time. Thus, the ferromagnetic $CrTe_2$ layer consists of approximately 16 monolayers (MLs). MFM images were taken at 2 K to investigate magnetic ground state of the $Bi_2Te_3/CrTe_2$ heterostructure after the sample was zero field cooled (ZFC) from room temperature. As shown in Fig. 1(e) the worm-like domain structure was observed at zero field. This is a typical domain pattern for ferromagnetic films with perpendicular uniaxial magnetic anisotropy. A line-cut through the magnetic domain structures reveals the representative domain size in the range around 0.6 μm–0.8 μm. External magnetic fields were applied to see how the magnetic domains evolve from the magnetic ground state, as shown in Fig. 2. At 0.15 T, the magnetic domain pattern is not changed significantly, because the magnetic field is not strong enough to flip the magnetic moments. However, the domain contrast was enhanced by ∼ 3.6 times, because of the enhanced MFM tip moments. Further increasing external fields results in a gradual reduction of the anti-parallel domain areas due to depinning of the domain boundaries. The magnetic worms shrink into magnetic bubbles as shown in Figs. 2(e)–2(i). The magnetic film was finally saturated at 1 T, as the pinned magnetic bubbles totally disappeared. In order to obtain the virgin magnetization (M–H) curve, the binary images with 0 and 1 elements (representing up and down domains) were calculated based on MFM images. Therefore, the normalized magnetization (M/M_s)

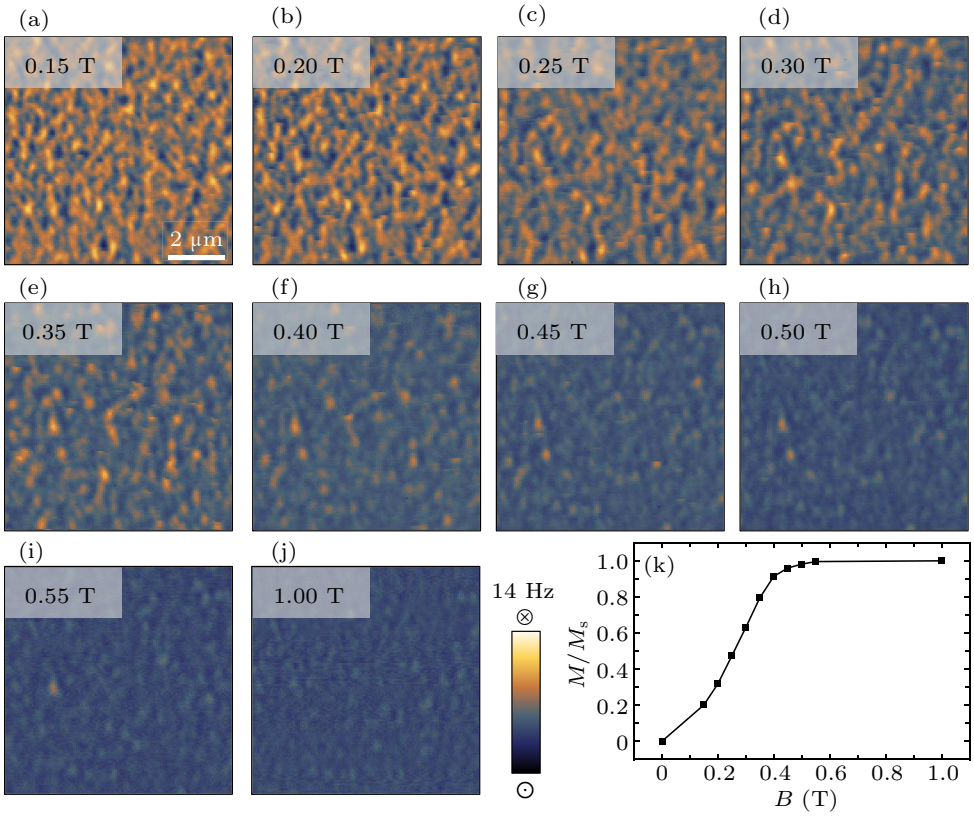


Fig. 2. (a)–(j) MFM images (2 K) taken at various magnetic fields from 0.15 T to 1.00 T after zero field cooling. The nominal fields were labelled at left upper corners of the MFM images. (k) The normalized magnetization estimated from MFM images at various magnetic fields.

can be estimated by using this following formula:

$$M/M_{\rm s} = \frac{N_{\rm up} - N_{\rm down}}{N_{\rm up} + N_{\rm down}}, \tag{1}$$

where $M_{\rm s}$ is the saturation magnetization, and $N_{\rm up}$ is the area of up domains, $N_{\rm down}$ is the area of down domains. By calculating the normalized magnetization at various magnetic fields, the $M/M_{\rm s}$–H curve was plotted in Fig. 2(k). It exhibits a domain-wall-type virgin magnetization curve, with a gradual increase of M at beginning. This indicates the domain wall pinning dominates the magnetization reversal process.

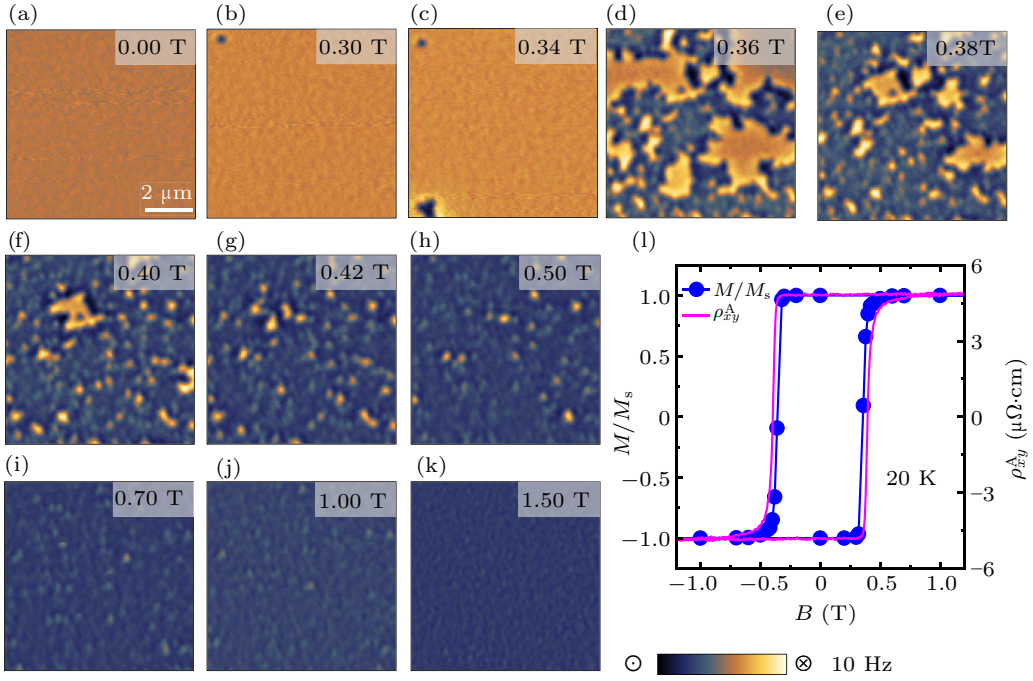


Fig. 3. (a)–(k) MFM images (20 K) taken at various magnetic fields. The nominal fields were labelled at right upper corners of the MFM images. (l) The solid blue circles represent $M/M_{\rm s}$–H data deduced from the MFM images. Note that another half is replicated from measured results via symmetry. The pink curve is the anomalous Hall resistance as a function of magnetic fields.

The field-sweeping MFM experiments were performed at 20 K to study the magnetization reversal process in the $Bi_2Te_3/CrTe_2$ heterostructure. The sample was fully magnetized at large negative magnetic fields at first. Then the field was ramped to zero and MFM images were taken. The film was maintained at the negatively magnetized state as shown in Fig. 3(a), indicating a strong perpendicular magnetic anisotropy (PMA). At 0.3 T and 0.34 T, nucleation of positively magnetized areas occurs at the upper left and lower left parts of the region, as shown in Figs. 3(b) and 3(c). Keeping increasing the magnetic field, the propagation of the magnetic domain walls could be observed and more areas were positively magnetized. The up and down domain areas were almost equally populated at 0.36 T and net magnetization were approaching zero, suggesting the coercive field at 20 K around 0.36 T. Note that the domain wall creeping is inevitable around coercive field, which is unfavorable for MFM imaging. To minimized domain wall creeping effect and the influence from magnetic tip stray field, all MFM images were taken at a small magnetic field of approximately 0.1 T after the magnetic field was ramped to the desired value. The pinned magnetic domain structures imaged around the coercive field show relatively large domain size around 2 μm–3 μm, in sharp contrast to the worm-like domain structures after ZFC. When the magnetic field was increased to 0.42 T, only small pinned magnetic bubbles could be seen and the $M/M_{\rm s}$ value is around 0.9, indicating the heterostructure was almost saturated. The ratio of coercive field to saturated field is around 0.86. This suggests a sharp magnetization reversal typical for a high-quality magnetic film with weak magnetic pinning. At 1.0 T, all pinned bubbles disappeared and the film was fully saturated. The square-like $M/M_{\rm s}$–H hysteresis loop was plotted in Fig. 3(l). In order to compare the local magnetic characterization with the bulk one, anomalous Hall measurements were performed on the same heterostructure. The raw Hall resistance was measured after antisymmetry operation to remove the longitudinal resistance. The total Hall effect consists of two contributions, ordinary Hall effect and anomalous Hall one:

$$R_{xy} = R^{\rm O}_{xy} + R^{\rm A}_{xy} = R_0 B + R_{\rm s} M, \tag{2}$$

where B is the magnetic field, R_0 is the ordinary Hall coefficient, $R_{\rm s}$ is the anomalous Hall coefficient, and M is the magnetization. After subtracting the ordinary Hall slope, the anomalous Hall contribution can be revealed, which is proportional to M. The anomalous Hall loop (pink curve), as shown

in Fig. 3(l), is in good agreement with the M/M_s–H loop estimated from MFM. This indicates the local MFM measurement is representative of the whole heterostructure and its magnetic property is relatively uniform. The variable-field MFM experiment was also performed at 100 K to investigate the temperature dependence. The magnetization reversal process shows similar ferromagnetic domain behavior with strong PMA, as shown in Fig. 4. Compared to 20-K experiments, more nucleation sites could be spotted at the early magnetization reversal processes, for instance, two nucleation sites appeared in Fig. 3(c) for 20-K experiments, while four sites appeared in Fig. 4(c) for 100-K one. This indicates the nucleation energy barrier is easier to overcome at elevated temperatures. The coercive field and magnetic signals at 100 K become smaller, i.e., H_c is almost halved, the MFM signal is reduced to roughly 0.7. The reduction of nucleation sites at higher temperatures have been also observed in other ferromagnetic thin films.[35]

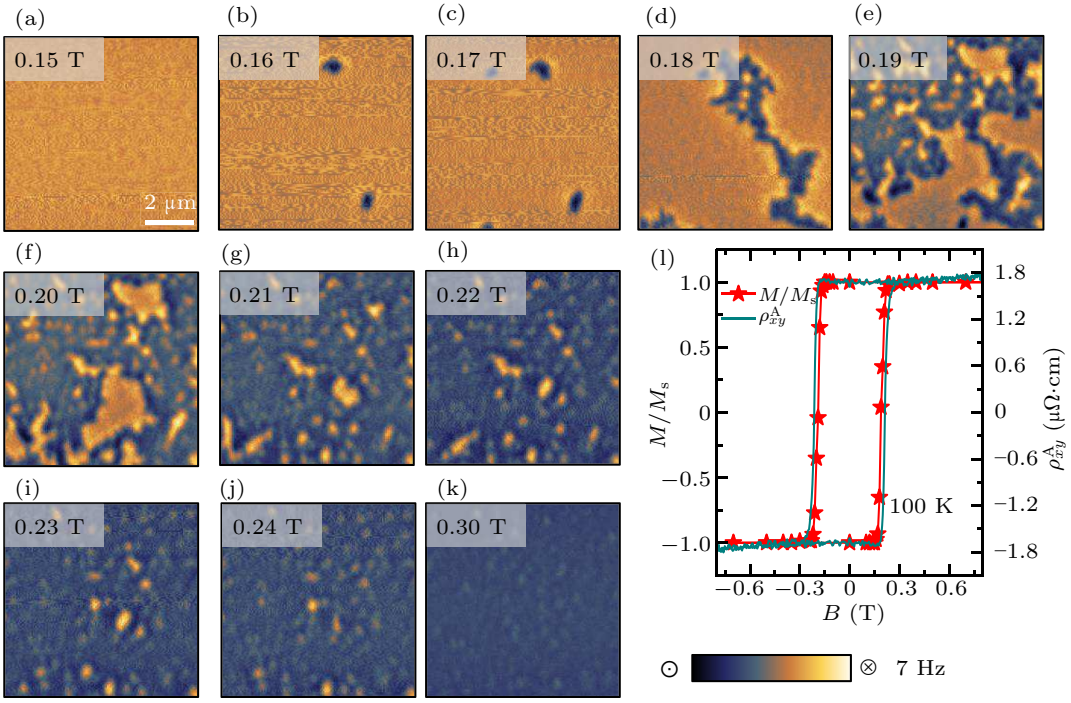


Fig. 4. (a)–(k) MFM images (100 K) taken at various magnetic fields. The nominal fields were labelled at left upper corners of the MFM images. (l) The solid red stars represent M/M_s–H data deduced from the MFM images. Note that another half is replicated from measured results via symmetry. The green curve is the anomalous Hall resistance as a function of magnetic fields.

Variable-temperature MFM measurements were conducted at zero magnetic field to study the ferromagnetic transition of the $Bi_2Te_3/CrTe_2$ heterostructure. We applied magnetic field at 0.4 T (around H_c) at 2 K, and then removed the field to induce large magnetic domains. As the temperature increases, the magnetic domain pattern was not altered significantly, while the domain contrast was indeed decreased, as shown in Figs. 5(a)–5(k). Around 200 K, the magnetic domain wall was blurred and only weak magnetic inhomogeneity was observable, indicating the melting of ferromagnetic order around Curie temperature. Further increasing the temperature drove a ferromagnetic to paramagnetic phase transition, and magnetic signal eventually disappeared. To quantitatively characterize the temperature-dependent magnetic domain contrast, the MFM signals from the up (blue box) and down (yellow box) domains were deduced:

$$\bar{f}_{\rm up} = \frac{1}{n^2}\sum_{i=1}^{n^2} f_i, \quad \bar{f}_{\rm down} = \frac{1}{n^2}\sum_{j=1}^{n^2} f_j,$$
$$\Delta f = \bar{f}_{\rm up} - \bar{f}_{\rm down},$$

where f_i is MFM signal (frequency shift) for each pixel, the pixel for blue and yellow square box is $n = 9$, domain contrast Δf means the average phase value $\bar{f}_{\rm up}$ in blue box minus the average phase value $\bar{f}_{\rm down}$ in yellow box. The error bar of Δf was calculated by the root-mean-square (RMS) values of the 9×9 pixels in the blue square:

$$\bar{f}_{\rm RMS} = \frac{1}{n^2}\sqrt{\sum_{i=1}^{n^2}\left(f_j - \bar{f}\right)^2}.$$

The temperature dependence of domain contrast from MFM images was plotted in Fig. 5(l). The temperature dependence curve can be nicely fitted by the mean-field theory for a Landau second-order phase transition: $M \propto (T_C - T)^{0.5}$. The nonlinear fitting gives the Curie temperature (T_C) of the $Bi_2Te_3/CrTe_2$ heterostructure around 201.5 K. The mean-field-like behavior of the ferromagnetic phase transition indicates a robust long-range ferromagnetic order in the heterostructure.

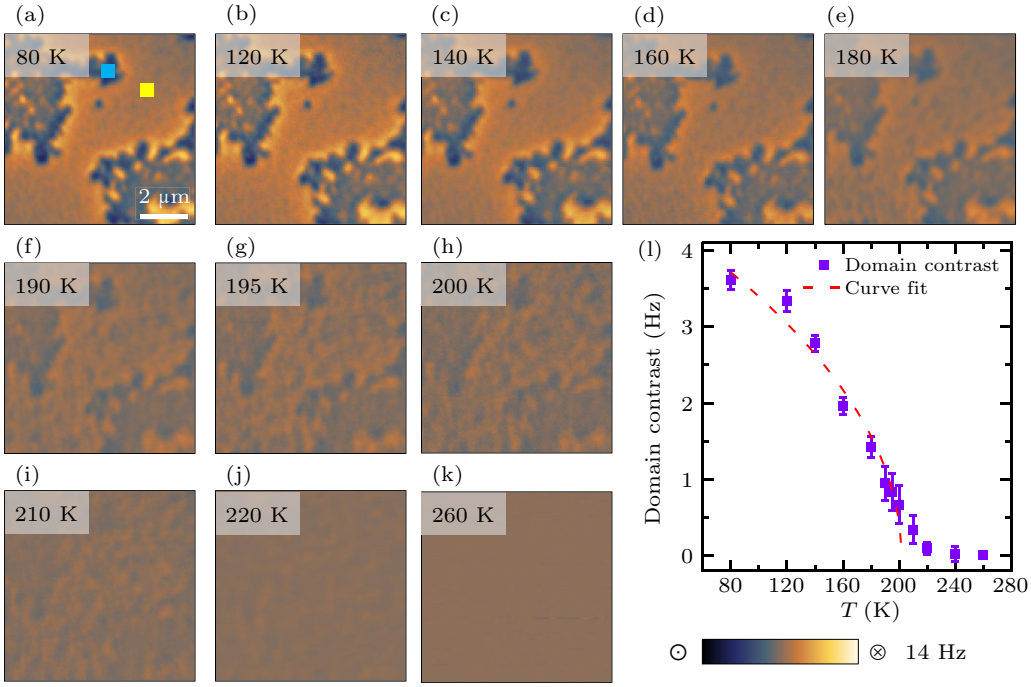


Fig. 5. (a)–(k) Zero-field MFM images of induced ferromagnetic domains measured at different temperatures. The nominal temperatures were labelled at left upper corners of the MFM images. (l) The purple points are the difference of MFM signals from blue and yellow boxes as shown in panel (a) at various temperatures. The red dashed line is the fitted curve based on mean-field theory.

4. Conclusion and perspectives

In conclusion, we systematically studied the magnetic domain structures of Bi_2Te_3 (20 nm)/$CrTe_2$(10 nm) heterostructure, which has shown excellent SOT switching performance. Worm-like sub-μm magnetic domains spontaneously form at its ground state after ZFC, while larger magnetic domains with a size around 2 μm–3 μm can be induced around coercive field during isothermal magnetization reversal process. The field and temperature dependence of the MFM images show a robust ferromagnetic ordering in this SOT device, which could be potentially utilized in MRAM. Up to now, the SOT switching of Bi_2Te_3/$CrTe_2$ heterostructure still requires an in-plane magnetic field, which is not favorable for industrial applications. The in-plane symmetry breaking can be artificially introduced by exchange coupling,[36,37] device asymmetry,[38,39] and structural dislocations.[40] Further MFM studies of the domain evolution during field-free SOT switching will be intriguing for material scientists to understand the underlying mechanism of SOT at microscopic scale.

Acknowledgements

Project supported by the National Key Research and Development Program of China (Grant No. 2022YFA1403000), the National Natural Science Foundation of China (Grant No. 12374161), and the Fund from the Science and Technology Commission of Shanghai Municipality (Grant No. 21PJ410800). X. F. Kou acknowledges the support from the National Natural Science Foundation of China (Grant No. 92164104), the RisingStar Program of Shanghai (Grant No. 21QA1406000), and the Open Fund of State Key Laboratory of Infrared Physics.

References

[1] Gong C, Li L, Li Z L, Stern A, Xia Y, Cao T, Bao W, Wang C Z, Wang Y, Qiu Z Q, Cava R J, Louie S G, Xia J and Zhang X 2017 *Nature* **546** 265
[2] Huang B V, Clark G, Navarro-Moratalla E, Klein D R, Cheng R, Seyler K L, Zhong D, Schmidgall E, McGuire M A, Cobden D H, Yao W, Xiao D, Jarillo-Herrero P and Xu X D 2017 *Nature* **546** 270
[3] Geim A K and Grigorieva I V 2013 *Nature* **499** 419
[4] Geisenhof F R, Winterer F, Seiler A M, Lenz J, Xu T Y, Zhang F and Weitz R T 2021 *Nature* **598** 53
[5] Cao Y, Fatemi V, Fang S, Watanabe K, Taniguchi T, Kaxiras E and Jarillo-Herrero P 2018 *Nature* **556** 43
[6] Park J M, Cao Y, Watanabe K, Taniguchi T and Jarillo-Herrero P 2021 *Nature* **590** 249
[7] Serlin M, Tschirhart C L, Polshyn H, Zhang Y, Zhu J, Watanabe K, Taniguchi T, Balents L and Young A F 2020 *Science* **367** 900
[8] Wu H, Zhang W, Yang L, Wang J, Li J, Li L, Gao Y, Zhang L, Du J, Shu H and Chang H 2021 *Nat. Commun.* **12** 5688
[9] Zhao D P, Zhang L G, Malik I A, Liao M H, Cui W Q, Cai X Q, Zheng C, Li L X, Hu X P, Zhang D, Zhang J X, Chen X, Jiang W J and Xue Q K 2018 *Nano Research* **11** 3116
[10] Wang M S, Kang L X, Su J W, Zhang L M, Dai H W, Cheng H, Han X T, Zhai T Y, Liu Z and Han J B 2020 *Nanoscale* **12** 16427
[11] Huang M, Wang S, Wang Z, Liu P, Xiang J, Feng C, Wang X, Zhang Z, Wen Z, Xu H, Yu G, Lu Y, Zhao W, Yang S A, Hou D and Xiang B 2021 *ACS Nano* **15** 9759
[12] Purbawati A, Coraux J, Vogel J, Hadj-Azzem A, Wu N, Bendiab N, Jegouso D, Renard J, Marty L, Bouchiat V, Sulpice A, Aballe L, Foerster M, Genuzio F, Locatelli A, Mentes T, Han Z, Sun X, Nunez-Regueiro M and Rougemaille N 2020 *ACS Appl. Mater. Interfaces* **12** 30702
[13] Sun X, Li W, Wang X, Sui Q, Zhang T, Wang Z, Liu L, Li D, Feng S, Zhong S, Wang H, Bouchiat V, Nunez Regueiro M, Rougemaille N, Coraux J, Purbawati A, Hadj-Azzem A, Wang Z, Dong B, Wu X, Yang T, Yu G, Wang B, Han Z, Han X and Zhang Z 2020 *Nano Research* **13** 3358

[14] Fabre F, Finco A, Purbawati A, Hadj-Azzem A, Rougemaille N, Coraux J, Philip I and Jacques V 2021 *Phys. Rev. Mater.* **5** 034008

[15] Xian J J, Wang C, Nie J H, Li R, Han M J, Lin J H, Zhang W H, Liu Z Y, Zhang Z M, Miao M P, Yi Y F, Wu S W, Chen X D, Han J B, Xia Z C, Ji W and Fu Y S 2022 *Nat. Commun.* **13** 257

[16] Zhang X, Lu Q, Liu W, Niu W Q, Sun J B, Cook J, Vaninger M, Miceli P F, Singh D J, Lian S W, Chang T R, He X, Du J, He L, Zhang R, Bian G and Xu Y 2021 *Nat. Commun.* **12** 2492

[17] Wen Y, Liu Z H, Zhang Y, Xia C X, Zhai B X, Zhang X H, Zhai G H, Shen C, He P, Cheng R Q, Yin L, Yao Y Y, Sendeku M G, Wang Z X, Ye X B, Liu C S, Jiang C, Shan C X, Long Y W and He J 2020 *Nano Lett.* **20** 3130

[18] Zhong Y, Peng C, Huang H L, Guan D D, Hwang J, Hsu K H, Hu Y, Jia C J, Moritz B, Lu D H, Lee J S, Jia J F, Devereaux T P, Mo S K and Shen Z X 2023 *Nat. Commun.* **14** 5340

[19] Zhang C H, Liu C, Zhang J W, Yuan Y Y, Wen Y, Li Y, Zheng D X, Zhang Q, Hou Z P, Yin G, Liu K, Peng Y and Zhang X X 2023 *Adv. Mater.* **35** 2205967

[20] Li B L, Deng X, Shu W N, Cheng X, Qian Q, Wan Z, Zhao B, Shen X H, Wu R X, Shi S, Zhang H M, Zhang Z C, Yang X D, Zhang J W, Zhong M Z, Xia Q L, Li J, Liu Y, Liao L, Ye Y, Dai L, Peng Y, Li B and Duan X D 2022 *Mater. Today* **57** 66

[21] Zhang L Z, Zhang A L, He X D, Ben X W, Xiao Q L, Lu W L, Chen F, Feng Z J, Cao S X, Zhang J C and Ge J Y 2020 *Phys. Rev. B* **101** 214413

[22] Tang B J, Wang X W, Han M J, Xu X D, Zhang Z W, Zhu C, Cao X, Yang Y M, Fu Q D, Yang J Q, Li X J, Gao W B, Zhou J D, Lin J H and Liu Z 2022 *Nat. Electron.* **5** 224

[23] Chen C, Chen X, Wu C, Wang X, Ping Y, Wei X, Zhou X, Lu J, Zhu L, Zhou J, Zhai T and Han J 2022 *Adv. Mater.* **34** 2107512

[24] Zhu W, Ma Z W, Yan J, Zheng G H, Cheng L, Xu X L, Meng Z, Shen L, An K Y, Zhou Ch, Qu Zh, Luo X, Sun Y P, Zhang Z J and Sheng Z G 2020 *J. Magn. Magn. Mater.* **512** 167019

[25] Wang Y, Yan, J, Li J, Wang S, Song M, Song J, Li Z, Chen K, Qin Y, Ling L, Du H, Cao L, Luo X, Xiong Y and Sun Y 2019 *Phys. Rev. B* **100** 024434

[26] Ma X, Huang M, Wang S S, Liu P, Zhang Y, Lu Y L and Xiang B 2023 *ACS Appl. Electron. Mater.* **5** 2838

[27] Ren Q D, Lai K, Chen J H, Yu X X and Dai J Y 2023 *Chin. Phys. B* **32** 027201

[28] Yuan Z Y, Yang F Z, Lv B Q, Huang Y B, Qian T, Xu J P and Ding H 2024 *Chin. Phys. B* **33** 026802

[29] Yang H, Valenzuela S O, Chshiev M, Couet S, Dieny B, Dlubak B, Fert A, Garello K, Jamet M, Jeong D E, Lee K, Lee T, Martin M B, Kar G S, Seneor P, Shin H J and Roche S 2022 *Nature* **606** 663

[30] Liu X Q, Huang P Y, XIA Y Y Y, Gao L, Liao Li Y, Cui B S, Backes D, van der Laan G, Hesjedal T, Ji Y C, Chen P, Zhang Y F, Wu F, Wang M X, Zhang J W, Yu G Q, Song C, Chen Y L, Liu Z K, Yang Y M, Peng Y, Li G, Yao Q and Kou X F 2023 *Adv. Funct. Mater.* **33** 2304454

[31] Ou Y, Yanez W, Xiao R, Stanley M, Ghosh S, Zheng B, Jiang W, Huang Y S, Pillsbury T, Richardella A, Liu C X, Low T, Crespi V H, Mkhoyan K A and Samarth N 2022 *Nat. Commun.* **13** 2972

[32] Zhang X Q, Ambhire S C, Lu Q S, Niu W, Cook J, Jiang J D S, Hong D S, Alahmed L, He L, Zhang R, Xu Y B, Zhang S S L, Li P and Bian G 2021 *ACS Nano.* **15** 15710

[33] Chen J S, Wang L J, Zhang M, Zhou L, Zhang R N, Jin L P, Wang X S, Qin H L, Qiu Y, Mei J W, Ye F, Xi B, He H T, Li B and Wang G 2019 *Nano Lett.* **19** 6144

[34] Jeon J H, Na H R, Kim H, Lee S, Song S, Kim J, Park S, Kim J, Noh H, Kim G, Jerng S K and Chun S H 2022 *ACS Nano* **16** 8974

[35] Wang W B, Mundy J A, Brooks C M, Moyer J A, Holtz M E, Muller D A, Schlom D G and Wu W D 2017 *Phys. Rev. B* **95** 134443

[36] Lau Y C, Betto D, Rode K, Coey J M D and Stamenov P 2016 *Nat. Nanotechnol.* **11** 758

[37] Fukami S, Zhang C L, DuttaGupta S, Kurenkov A and Ohno H 2016 *Nat. Mater.* **15** 535

[38] Yu G Q, Upadhyaya P, Fan Y B, Alzate J G, Jiang W J, Wong K L, Takei S, Bender S A, Chang L T, Jiang Y, Lang M R, Tang J S, Wang Y, Tserkovnyak Y, Amiri P K and Wang K L 2014 *Nat. Nanotechnol.* **9** 548

[39] Liu L, Qin Q, Lin W N, Li C, Xie Q, He S, Shu X, Zhou C H, Lim Z, Yu J, Lu W, Li M, Yan X B, Pennycook S J and Chen J S 2019 *Nat. Nanotechnol.* **14** 939

[40] Liang Y H, Yi D, Nan T X, Liu S S, Zhao L, Zhang Y J, Chen H T, Xu T, Dai M Y, Hu J M, Xu B, Shi J, Jiang W J, Yu R and Lin Y H 2023 *Nat. Commun.* **14** 5458